



Effects of electron-withdrawing group and electron-donating core combinations on physical properties and photovoltaic performance in D- π -A star-shaped small molecules

Yuriy N. Luponosov^{a,*}, Jie Min^{b,**}, Alexander N. Solodukhin^a, Oleg V. Kozlov^{c,d}, Marina A. Obrezkova^a, Svetlana M. Peregudova^{a,e}, Tayebah Ameri^b, Sergei N. Chvalun^{a,f}, Maxim S. Pshenichnikov^c, Christoph J. Brabec^{b,g}, Sergei A. Ponomarenko^{a,h}

^a Enikolopov Institute of Synthetic Polymeric Materials of the Russian Academy of Sciences, Profsoyuznaya st. 70, Moscow, 117393, Russia

^b Institute of Materials for Electronics and Energy Technology (i-MEET), Friedrich-Alexander-University Erlangen-Nuremberg, Martensstraße 7, 91058, Erlangen, Germany

^c Zernike Institute for Advanced Materials, University of Groningen, Nijenborgh 4, 9747 AG, Groningen, The Netherlands

^d Faculty of Physics & International Laser Center, Lomonosov Moscow State University, Leninskie Gory 1, 119991, Moscow, Russia

^e Nesmeyanov Institute of Organoelement Compounds, Russian Academy of Sciences, Vavilova St. 28, Moscow, 119991, Russia

^f National Research Centre "Kurchatov Institute", 1, Akademika Kurchatova pl., Moscow, 123182, Russia

^g Bavarian Center for Applied Energy Research (ZAE Bayern), Haberstraße 2a, 91058, Erlangen, Germany

^h Chemistry Department, Moscow State University, Leninskie Gory 1-3, Moscow, 119991, Russia

ARTICLE INFO

Article history:

Received 14 December 2015

Received in revised form

15 February 2016

Accepted 15 February 2016

Available online xxx

Keywords:

Star-shaped molecules

3-Ethylrhodanine

Triphenylamine

Dicyanovinyl

Organic solar cells

Ultrafast charge separation

ABSTRACT

The first representatives of star-shaped molecules having 3-alkylrhodanine (alkyl-Rh) electron-withdrawing groups, linked through bithiophene π -spacer with electron-donating either triphenylamine (TPA) or *tris*(2-methoxyphenyl)amine (m-TPA) core were synthesized. The physical properties and photovoltaic performance of these novel molecules with 3-ethylrhodanine groups were comprehensively studied and compared to their full analogs having dicyanovinyl (DCV) units as the other type of well-known and frequently used acceptor groups. On one hand, the former demonstrate several advantages such as higher solubility and better photovoltaic performance in bulk-heterojunction (BHJ) organics solar cells (OSCs) as compared to the latter. Nevertheless, the former have slightly lower optical/electrochemical bandgaps and higher thermooxidation stability. On the other hand, molecules of both series based on m-TPA core along with higher solubility and higher position of HOMO energy levels have more pronounced tendency to crystallize as compared to the TPA-based molecules. Detailed investigation of the structure-property relationships for these series of molecules revealed that donor and acceptor unit combinations influence both charge generation and charge transport/recombination properties, as demonstrated by the ultrafast photoinduced absorption spectroscopy, space charge limited current measurements and transient photovoltage technique. These results give more insight how to fine-tune and predict physical properties and photovoltaic performance of small molecules having either alkyl-Rh or DCV units in their chemical structures and thus providing a molecular design guideline for the next generation of high-performance photovoltaic materials.

© 2016 Elsevier B.V. All rights reserved.

1. Introduction

Among all available renewable energy sources, solar energy appears to be the most promising primary energy source of the

future [1]. Organic solar cells (OSCs) excel with low production costs, substrate and shape freedom, and the ability to manufacture lighter, highly flexible, and semitransparent devices, which open avenues for new application areas such as building integrated photovoltaics for sun shading and electricity generating glass facades [2,3]. Solution-processable small molecules for bulk heterojunction (BHJ) OSCs have attracted considerable attention in recent years because of their advantages of high purity, definite molecular

* Corresponding author.

** Corresponding author.

E-mail addresses: luponosov@ispm.ru (Y.N. Luponosov), Min.Jie@fau.de (J. Min).

weight, and low cost [4,5]. Although optimized solution-processed OSCs based on small-molecule donor materials blended with fullerene acceptors achieved the efficiencies over 10% [6], development of the cheap and stable photoactive materials as well as novel design strategies for small molecules is still a key to boost potential for commercial applications.

Donor-acceptor (D–A) approach is a successful tool to design small molecules possessing broadened absorption spectra, high hole mobility, and suitable energy levels of frontier molecular orbitals [7,8]. D–A molecules having star-shaped [9] or linear [4–6] symmetric architecture are the most frequently used types of materials for solution-processed OSCs. Recent studies revealed that the properties of small molecules both in pristine and in blended state are very sensitive to even minimal changes in their chemical structures, such as a length and position of alkyl group [9–12], length and nature of π -bridge [13–16], heteroatom substitution [17,18] etc. However, some basic parameters of the D–A molecules, such as optical absorption range, energy levels, electrochemical stability etc. are specified mainly by the nature of D and A unit combinations. Therefore, there is an urgent need for investigating the effect of D and A unit combination in small molecules, which can provide a more detailed insight into their structure-property relationships and subtle design strategies.

Recently, OSCs based on D–A small molecules containing 3-alkylrhodanine (alkyl-Rh) groups as electron-withdrawing units have demonstrated record high efficiencies [19]. The promising results on the linear small molecules demonstrated that alkyl-Rh group is an excellent acceptor unit that probably can also be useful in other systems. To our best knowledge, star-shaped D–A molecules with alkyl-Rh groups have not been reported yet, whereas the star-shaped architecture has a number of attractive advantages over the linear one, such as higher solubility, better film-forming properties, less anisotropy of optical and electrical properties, increased number of pathways for light conversion, etc. [20–22]. There is only one recent report on the synthesis of star-shaped molecule with a modified rhodanine group, 2-(1,1-dicyanomethylene)-3-octyl [23].

Nowadays, the most attractive star-shaped molecules for OSCs are based on triphenylamine (TPA) as the donor and dicyanovinyl (DCV) as the acceptor unit due to their low cost, well-established chemistry, excellent physical and chemical properties [21,24]. Recently we have systematically investigated various properties of this type of star-shaped molecules depending on the length and position of alkyl group as well as length of π -bridge [9,11,14]. More recently, our works have demonstrated that usage of *tris*(2-methoxyphenylamine) (m-TPA), being an analog of TPA with methoxy substitutes, to design star-shaped molecules with DCV groups leads to an increased molecular solubility and crystallinity without a loss in photovoltaic performance [25,26]. Besides DCV, benzothiadiazole [27,28] and 2-ethylhexyl cyanoacetate [29] are frequently used acceptor blocks to design efficient TPA-based star-shaped materials for OSCs. In addition, the effect of peripheral acceptor group, such as DCV, indanedione, 2-ethylhexyl cyanoacetate and 1,3-diethyl-2-thiobarbituric in star-shaped TPA-based symmetrical [30] and unsymmetrical [31,32] molecules were investigated and showed a great influence of such modifications on their photophysical properties. Nonetheless, despite all these promising results, there is still a vast space for material scientists to modify and improve the physical parameters and photovoltaic efficiency of star-shaped molecules by smartly gaming D and A unit combinations.

In this paper, two novel star-shaped molecules, namely N(Ph-2T-Rh-Et)₃ and N(Ph-OMe-2T-Rh-Et)₃, with 3-ethylrhodanine (Rh-Et) as the acceptor groups and either TPA or m-TPA as the donor core were designed and synthesized (Scheme 1). Comprehensive

study of thermal, optical and electrochemical properties, film morphology, charge generation, charge transport and recombination properties, as well as photovoltaic performance of these molecules in comparison to their full analogs having frequently-used DCV groups, N(Ph-2T-DCV)₃ and N(Ph-OMe-2T-DCV)₃, allows to evaluate benefits and drawbacks for each of the D–A combination.

2. Results and discussion

2.1. Synthesis and chemical characterization

Synthesis of the star-shaped molecules with 3-ethylrhodanine groups is outlined in Scheme 2. First, star-shaped precursors with 5,5-dimethyl-1,3-dioxane-protected carbonyl functions **3a** and **3b** were prepared via Suzuki coupling between the pinacol boronic ester of 2,2-bithiophene derivative (**1**) and *tris*(4-bromophenyl)amine (**2a**) or *tris*(4-bromo-2-methoxyphenyl)amine (**2b**) respectively in 81–83% isolated yields. Removing the protective groups was successfully achieved by treatment of the acetals with 1 M HCl to give corresponding aldehydes (**4a–b**) in 95–99% isolated yields. Finally, N(Ph-2T-Rh-Et)₃ and N(Ph-OMe-2T-Rh-Et)₃ were prepared by Knövenagel condensation of compounds **4a** and **4b** with N-ethylrhodanine in 50% and 65% isolated yields, respectively. To our best knowledge, N(Ph-2T-Rh-Et)₃ and N(Ph-OMe-2T-Rh-Et)₃ are the first representatives of D- π -A star-shaped molecules with alkylrhodanine groups. Preparation of their full analogs with terminal DCV groups, N(Ph-2T-DCV)₃ [9] and N(Ph-OMe-2T-DCV)₃ [26], is described elsewhere and based on the similar synthetic approach.

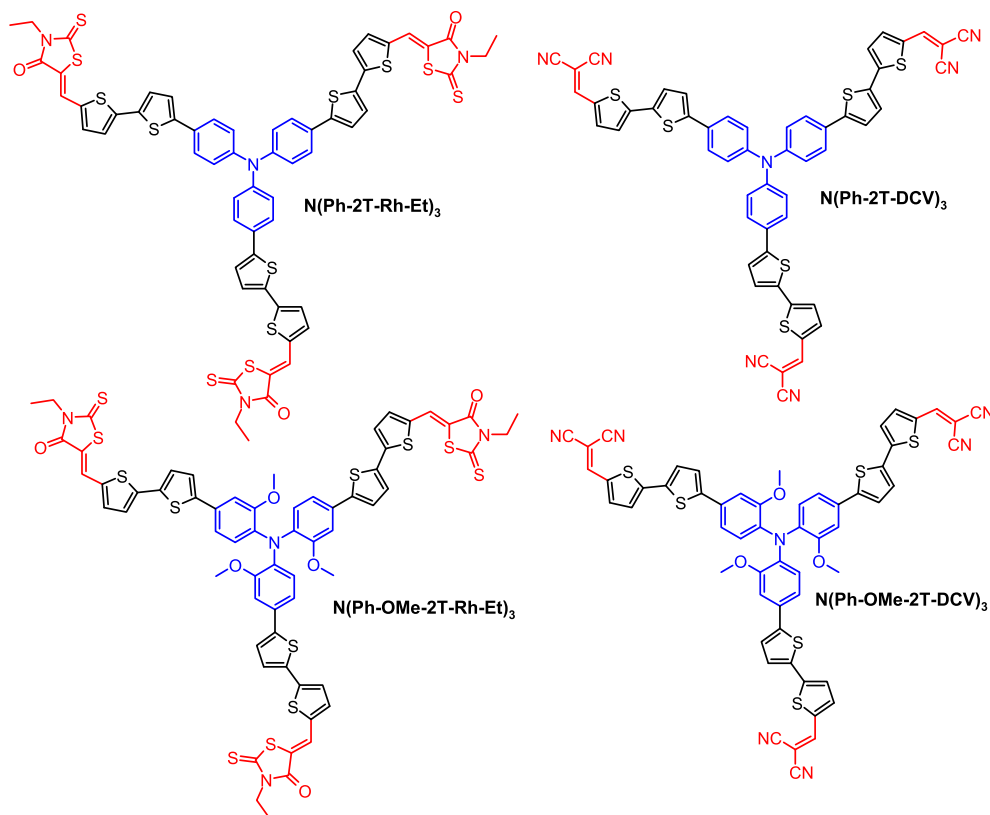
¹H-, and ¹³C NMR spectroscopy, elemental analysis, and mass-spectroscopy were used to characterize chemical structure of the precursors and final compounds (see Experimental part and Supporting Information, Fig. S1–S6). The oligomers obtained demonstrate moderate solubility in common organic solvents such as tetrahydrofuran (THF), chloroform, and 1,2-dichlorobenzene (ODCB) etc.

The accurate solubility values were measured in ODCB at room temperature (see Table 1). One can see that solubility of the star-shaped molecules with Rh-Et groups is higher as compared to their analogs with DCV groups. In addition, usage of m-TPA instead of TPA core also leads to increased solubility, which is in agreement with our previous results [25]. These observations can be explained by decreased intermolecular interactions for the small molecules having additional aliphatic or methoxy substitutes in their chemical structures.

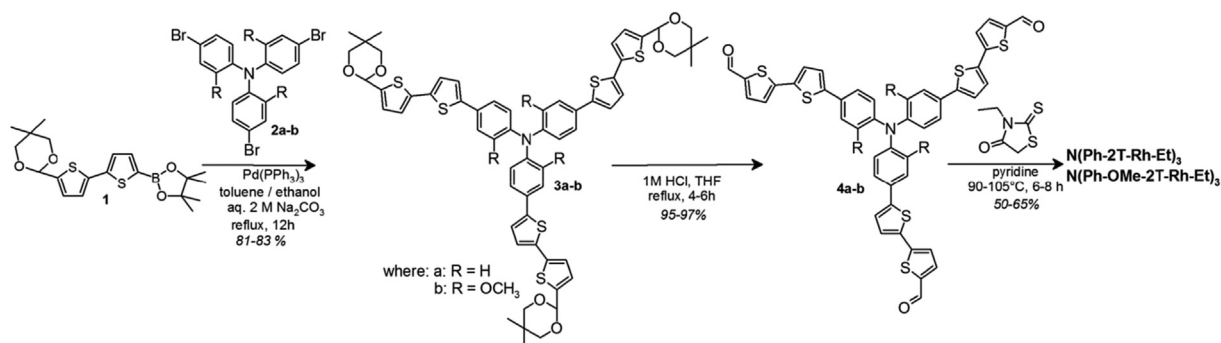
2.2. Thermal properties

Thermal properties of these four compounds were investigated by thermogravimetric analysis (TGA) and differential scanning calorimetry (DSC). The results are shown in Figs. 1 and 2, respectively, and summarized in Table 1.

One can see that all oligomers under consideration possess very high stability above 380 °C both in the air (Fig. 1a) and under inert atmosphere (Fig. 1b). However, there is some dependence of the decomposition temperature (T_d , corresponding to 5% weight losses) upon their chemical structure. Comparison of the character and percentage of the weight losses at 400–550 °C region for all these molecules indicates that it is caused mostly by the decomposition of the acceptors either DCV or 3-ethylrhodanine groups. The star-shaped molecules with 3-ethylrhodanine groups have slightly lower T_d in air as compared to those of DCV based molecules. This fact can be explained by presence of the aliphatic group in 3-ethylrhodanine unit, which probably decomposes first at high temperatures in the presence of oxygen. In addition, comparison of the residual coke at high-temperature region (450–550 °C) relative



Scheme 1. Chemical structures of D- π -A star-shaped molecules investigated in this work.



Scheme 2. Synthesis of the star-shaped molecules with 3-ethylrhodanine groups.

Table 1
Solubility and thermal properties of the star-shaped molecules investigated.

Compounds	Solubility, g L ⁻¹ ^a	First heating		Second heating		TGA (air)		TGA (N ₂)	
		T _m , °C	ΔH _m , J/g	T _g , °C	dC _p , J/(g·K)	T _d , °C	T _d , °C		
N(Ph-2T-Rh-Et) ₃	8	—	—	146	0.25	393	408		
N(Ph-2T-DCV) ₃ ^b	2	276	28	146	0.29	406	407		
N(Ph-OMe-2T-Rh-Et) ₃	11	266	45	143	0.24	386	400		
N(Ph-OMe-2T-DCV) ₃ ^c	9	200	32	147	0.33	401	408		

T_m – melting temperature; ΔH_m – melting enthalpy; T_g – glass transition temperature; ΔC_p – heat capacity change at the T_g; T_d – decomposition temperature (at 5% weight-loss).

^a Measured in ODCB.

^b Data from Ref. [9].

^c Data from Ref. [26].

to the nature of branching core revealed that the molecules with m-TPA core have larger weight losses, because of elimination of the methoxy substitutes.

DSC scans at first heating (Fig. 2a) revealed that molecules with DCV groups can be obtained as crystalline materials from solution [26] as opposite to compounds with 3-ethylrhodanine groups. It is

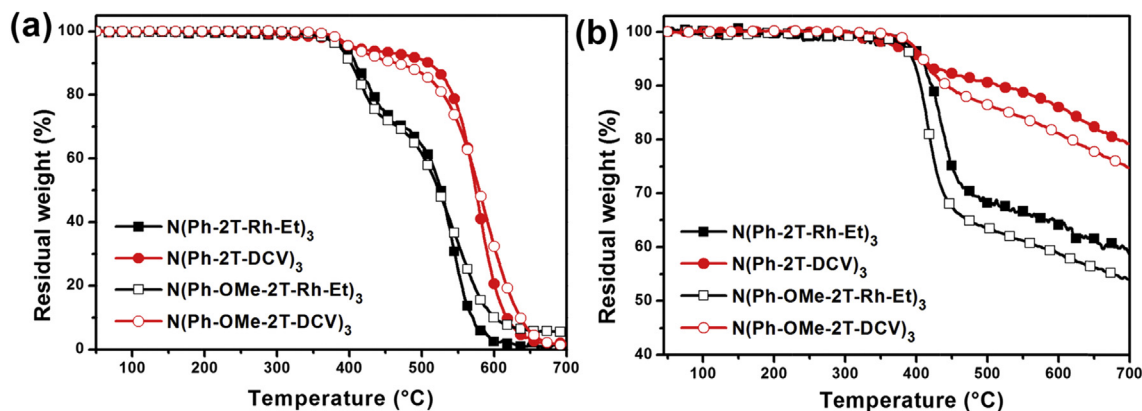


Fig. 1. TGA of D- π -A star-shaped molecules in (a) air and (b) nitrogen.

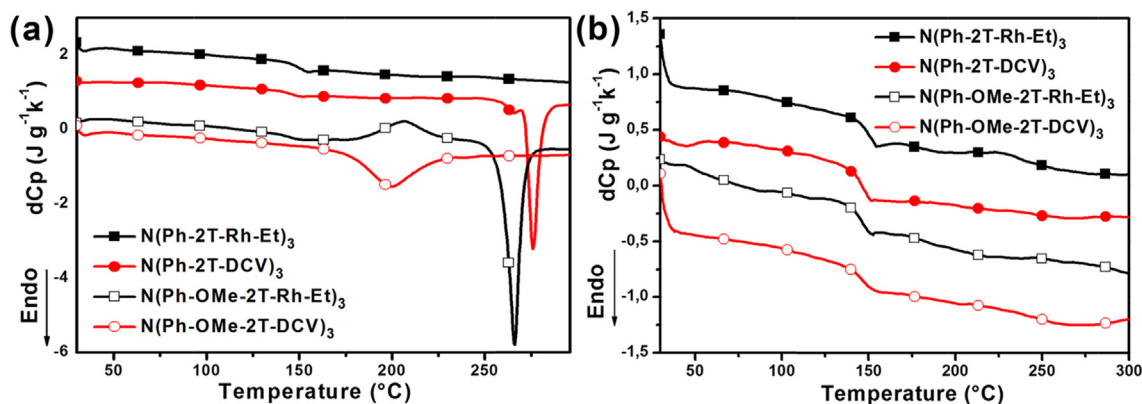


Fig. 2. DSC first (a) and second (b) heating scans of D- π -A star-shaped molecules.

interesting to note that at the first heating $N(\text{Ph-2T-Rh-Et})_3$ has the glass transition only, whereas its analog with *m*-TPA core, namely $N(\text{Ph-OMe-2T-Rh-Et})_3$, has an exothermic phase transition above the glass transition (180–220 °C), corresponding to a crystallization followed by melting at 276 °C. This indicates that *m*-TPA core can stimulate crystallization as compared to TPA core, which is in a good agreement with our previous results [26]. However, for the $N(\text{Ph-2T-DCV})_3/N(\text{Ph-OMe-2T-DCV})_3$ pair we observe an opposite effect. $N(\text{Ph-2T-DCV})_3$ has sharper endothermic peak at higher temperature and with larger value of melting enthalpy, which indicate its higher crystallinity as compared to $N(\text{Ph-OMe-2T-DCV})_3$. Nevertheless, all molecules under discussion become amorphous at cooling from the melt as it is evidenced by the second heating DSC scans (Fig. 2b) similar to other known TPA-based molecules, since a propeller-like TPA core hinders crystallization [24,26]. Interestingly, glass transition temperatures (T_g) were found to be very similar for all four molecules investigated in this work without pronounced reference to the type of donor or acceptor units.

2.3. Optical and electrochemical properties

UV-Vis absorption spectra of the star-shaped molecules in dilute ODCB solutions and in thin films are shown in Fig. 3 and the corresponding optical data are collected in Table 2. The shape of absorption spectra in solution is similar for all molecules investigated (Fig. 3a). Usually the UV absorption peaks at the high-energy region (ca. 400 nm) are ascribed to the π - π^* transitions, whereas the intensive visible absorption peaks in low-energy region are

attributed to the intramolecular charge-transfer (ICT) transition between donor and acceptor groups [31]. However, our recent work revealed that both bands have a mixed character and the intensity of the high-energy absorption feature is a direct measure of the degree of conformational disorder in the star-shaped molecule [33]. The molecules having *m*-TPA core demonstrate slightly red-shifted absorption spectra as compared to the analogs with TPA, especially in the case of $N(\text{Ph-2T-DCV})_3/N(\text{Ph-OMe-2T-DCV})_3$ pair. This can be explained by the fact that *m*-TPA core possesses stronger electron-donating ability as compared to TPA unit, resulting from the presence of electron-rich methoxy substitutes, which in turn leads to more pronounced ICT effect for the molecules with *m*-TPA core.

In thin films, similar tendencies are observed together with an obvious red-shift and broadened absorption as compared to the spectra in solution. In general, the spectra of the molecules with *m*-TPA core tend to be more red-shifted and broadened, which is more pronounced for $N(\text{Ph-2T-Rh-Et})_3/N(\text{Ph-OMe-2T-Rh-Et})_3$ pair, where the latter has 21 nm red-shift of the absorption maximum. The lower aggregation ability for $N(\text{Ph-2T-Rh-Et})_3$ in this pair as well as in the entire series of the molecules investigated can be explained by its amorphous nature according to the DSC data discussed above. In addition, the optical band gaps (E_g^{opt}) of $N(\text{Ph-2T-Rh-Et})_3$, $N(\text{Ph-2T-DCV})_3$, $N(\text{Ph-OMe-2T-Rh-Et})_3$ and $N(\text{Ph-OMe-2T-DCV})_3$ as calculated from the onset of the film absorption are estimated to be 1.77, 1.78, 1.68 and 1.72 eV, respectively. Considering these values together with the fact that the most red-shifted absorption maxima both in solutions and in thin films were found for the molecules having DCV groups, one can conclude that the molecules with DCV groups have slightly stronger character of ICT

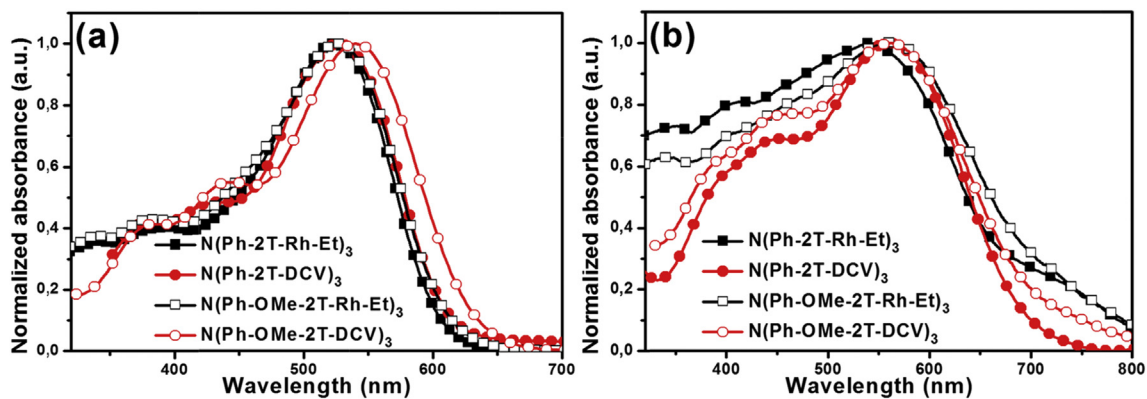


Fig. 3. UV-vis absorption spectra of star-shaped molecules in (a) dilute ODCB solutions and in (b) films cast from ODCB.

Table 2
Optical and electrochemical properties of the star-shaped molecules investigated.

Compounds	UV-vis absorption				Cyclic voltammetry		
	Solution ^a		Film ^b		Oxidation	Reduction	E_g^{EC} (eV)
	λ_{max} (nm)	λ_{max} (nm)	λ_{onset} (nm)	E_g^{opt} (eV) ^c	ϕ_{ox}^d /HOMO (V)/(eV)	ϕ_{red}^d /LUMO (V)/(eV)	
N(Ph-2T-Rh-Et) ₃	524	541	700	1.77	0.90/−5.30	−0.98/−3.42	1.88
N(Ph-2T-DCV) ₃ ^e	528	560	698	1.78	0.92/−5.32	−0.91/−3.49	1.83
N(Ph-OMe-2T-Rh-Et) ₃	527	562	738	1.68	0.82/−5.22	−1.02/−3.38	1.84
N(Ph-OMe-2T-DCV) ₃ ^f	540	561	720	1.72	0.80/−5.20	−0.94/−3.46	1.74

^a Measured in ODCB solution.

^b Cast from ODCB solution.

^c Bandgap estimated from the onset wavelength (λ_{edge}) of the optical absorption: $E_g^{opt} = 1240/\lambda_{edge}$.

^d Standard formal reduction (ϕ_{red}) and oxidation (ϕ_{ox}) potentials vs. SCE.

^e Data from Ref. [9].

^f Data from Ref. [26].

between the donor and acceptor units as compared to the molecular systems with alkyl-Rh groups, which is in a good agreement with electrochemical data as discussed below.

Electrochemical properties of the oligomers were investigated using cyclic voltammetry (CV) (see Fig. 4 and Table 2). Oxidation in ODCB–acetonitrile mixture occurs in two consecutive and fully reversible stages for the oligomers under discussion. However, in solid the oxidation of the molecules with alkyl-rhodanine groups becomes irreversible as compared to N(Ph-2T-DCV)₃ and N(Ph-OMe-2T-DCV)₃ (Fig. 4a). This phenomenon can be attributed to a stacking in the solid state of rhodanine-containing oligomers [34]. Interestingly, the particular type of acceptor group does not

influence the first oxidation potentials, whereas presence of additional electron-donating substituents at TPA core, such as methoxy group, facilitates the oxidation. These facts indicate that thienophenylamine fragments are mainly responsible for the oxidation in these molecules.

Apart from the oxidation, reduction of all these star-shaped molecules was found to be irreversible in both solution and solid, which can be attributed to the instability of their anion-radicals due to presence of the active proton at DCV and alkyl-Rh groups. It is known that substitution of the active vinyl proton to an alkyl group can stabilize the anion-radicals leading to the reversible or quasi-reversible reduction processes [9,35]. In this series of molecules,

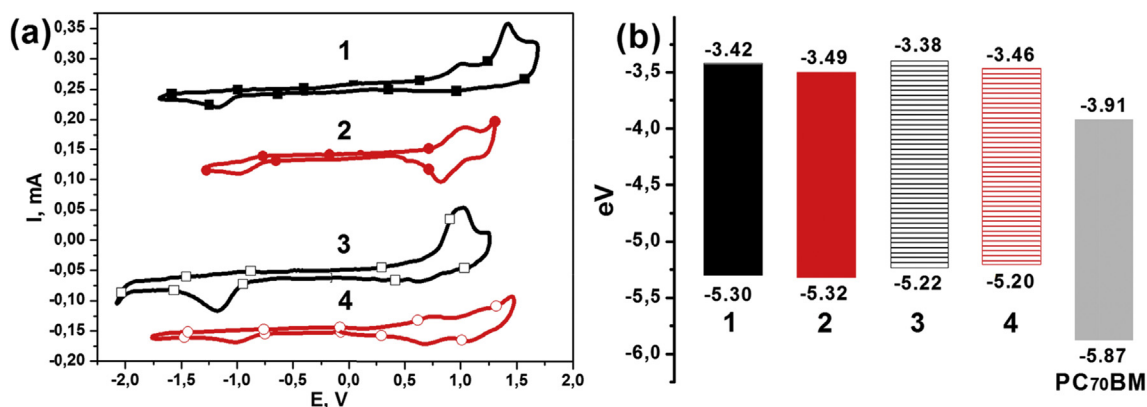


Fig. 4. (a) Cyclic voltammograms of films and (b) HOMO/LUMO energy levels diagrams of N(Ph-2T-Rh-Et)₃ (1), N(Ph-2T-DCV)₃ (2), N(Ph-OMe-2T-Rh-Et)₃ (3) and N(Ph-OMe-2T-DCV)₃ (4) in comparison to PC₇₀BM [36].

replacement of DCV by alkyl-Rh groups leads to a shift of the reduction potentials to the cathode region and hereby hinders reduction of the latter. Meanwhile, the reduction potentials were found to be not depended on the nature of donor core, confirming that the electron density is localized at the terminal electron-deficient either DCV or alkyl-Rh groups.

The highest occupied molecular orbital (HOMO) and lowest unoccupied molecular orbital (LUMO) energy levels were calculated using the first standard formal oxidation and reduction potentials obtained from the CV experiments in solids (see Table 2 and Fig. 4b). As expected, HOMO energy levels of the molecules with m-TPA core, N(Ph-OMe-2T-Rh-Et)₃ and N(Ph-OMe-2T-DCV)₃, were found to be higher as compared to their analogs having common TPA core without additional electron-donating methoxy groups. LUMO energy levels of the molecules with alkyl-Rh groups are slightly higher of those calculated for their analogs with DCV units. Considering bandgap values (E_g) of the molecules, one can conclude that usage of DCV group or m-TPA core for the molecular design of the small molecules leads to a slight decrease of E_g . Therefore, the lowest E_g (1.74 eV) was found for N(Ph-OMe-2T-DCV)₃, which corresponds well with the optical data (Table 2).

2.4. Photovoltaic properties of BHJ devices

Solution-processed BHJ OSCs were fabricated using [6,6]-Phenyl C₇₁ butyric acid methyl ester (PC₇₀BM) as the electron acceptor with conventional device structure of ITO/PEDOT:PSS/star-shaped molecules:PC₇₀BM/ZnO(ca. 25 nm)/Al(100 nm), and the detailed device fabrication process is described in the Experimental section. The corresponding parameters of the devices with optimized blending ratios and without any post-treatments are summarized in Fig. S7 and Table 3. The best current density-voltage (J - V) curves and external quantum efficiency (EQE) spectra of the related devices are shown in Fig. 5a and b, respectively.

Due to their low-lying HOMO energy levels (see Table 2), OSCs based on these star-shaped molecules show relatively high open-circuit voltage (V_{oc}) of over 0.90 V as expected. Furthermore, we found that OSCs based on N(Ph-OMe-2T-Rh-Et)₃ and N(Ph-OMe-2T-DCV)₃ showed lower V_{oc} of 0.92 V and 0.90 V, respectively, as compared to those of TPA based molecules. These results are consistent with HOMO level variations, originating from the stronger electron-donating ability of m-TPA core. OSCs based on molecules with Rh-Et acceptor groups (N(Ph-2T-Rh-Et)₃ and N(Ph-OMe-2T-Rh-Et)₃) exhibited higher V_{oc} values as compared to the DCV based molecules (N(Ph-2T-DCV)₃ and N(Ph-OMe-2T-DCV)₃), probably due to the slightly lower electron-withdrawing ability of Rh-Et group as well as the morphological characteristics. In addition, as compared to the N(Ph-2T-DCV)₃ based devices, OSCs based on N(Ph-2T-Rh-Et)₃ provide a higher short circuit current density (J_{sc}) of 9.1 mA cm⁻² and a better fill factor (FF) of 45.6%.

Absorption spectra and electronic structure of the components are generally important for device operation, but here the role of

film morphology cannot be ignored [14]. The lower photovoltaic performance of N(Ph-2T-DCV)₃ based devices can be attributed to the insufficient solubility (2 mg mL⁻¹ in ODCB), probably resulting in the nonoptimal nanomorphology, which cannot be detected by the top atomic force microscopy (AFM) surface image (see Fig. S8). N(Ph-2T-Rh-Et)₃ and N(Ph-2T-DCV)₃ based blended films show smooth surfaces without any remarkable features at the resolution of the AFM, but the AFM images of the N(Ph-2T-Rh-Et)₃ based film exhibit larger interconnected regions and domains compared with N(Ph-2T-DCV)₃ film image. In contrast, N(Ph-OMe-2T-Rh-Et)₃ and N(Ph-OMe-2T-DCV)₃ based devices without a solubility issue showed the comparable photovoltaic parameters with the similar J_{sc} values (8.6 mA cm⁻² vs. 8.5 mA cm⁻²) as well as a slight difference of FF values (50.3% vs. 46.6%). It was also found that these two systems show similar morphology characteristic as demonstrated by AFM measurements (see Figure S8c and S8d). This suggests good dispersion of both molecules in the blend, but does not explain the difference in their photovoltaic performance.

Finally, the PCEs of these devices are 4.0% for N(Ph-2T-Rh-Et)₃, 2.4% for N(Ph-2T-DCV)₃, 4.0% for N(Ph-OMe-2T-Rh-Et)₃ and 3.6% for N(Ph-OMe-2T-DCV)₃. As an obvious result, photovoltaic performance of the OSCs based on the molecules with alkyl-Rh groups exceeds those of the devices with DCV groups. The external quantum efficiency (EQE) of the corresponding devices is shown in Fig. 5b, a broad spectral response across the wavelength range of 300–700 nm was observed for all devices. J_{sc} values calculated from the EQE spectra are 8.0 mA cm⁻² for N(Ph-2T-Rh-Et)₃, 5.7 mA cm⁻² for N(Ph-2T-DCV)₃, 7.5 mA cm⁻² for N(Ph-OMe-2T-Rh-Et)₃, 7.6 mA cm⁻² for N(Ph-OMe-2T-DCV)₃, respectively, which are in good agreement with the relevant J_{sc} values measured under simulated AM 1.5, in air. The slightly lower J_{sc} values obtained from the EQE measurements are caused either by device degradation during the measurements or by an underestimated spectral mismatch factor.

2.5. Charge transport

To gain further insights into the effects of nature of donor and acceptor unit combinations within structurally well-defined star-shaped molecules on the charge transport as well as the related structure-property relationships, space charge limited current (SCLC) method was used to map out hole and electron only mobilities of the blended films. The structures of hole and electron only devices were ITO/PEDOT:PSS/blended films/MoO₃ (15 nm)/Ag (100 nm) and ITO/ZnO/blended films/Ca (15 nm)/Ag (100 nm), respectively. Here, the charge carrier mobilities are measured by analyzing the dark current density-voltage (J - V) characteristics of single carrier devices. The related average values of hole only and electron only mobilities of blended films calculated by six diodes are shown in Fig. 6 and Table 4.

Obviously, N(Ph-2T-DCV)₃ shows the lowest hole only mobility in these blended films. Similarly, the electron only mobility (μ_e) of the devices based on N(Ph-2T-DCV)₃ as donor also exhibits the lowest value of 2.5×10^{-4} cm² V⁻¹ s⁻¹. Although N(Ph-2T-DCV)₃ blended films possessed the comparable μ_e/μ_h ratio as compared to the other three systems (see Table 4), the lower charge carrier mobilities in blended films resulted in the poor photovoltaic performance as mentioned above. It should be noted here that the poor charge transport properties in N(Ph-2T-DCV)₃ blended films can be attributed to the morphological characteristics due to the insufficient molecule solubility. In order to reduce the negative effects of poor solubility, introducing a more soluble m-TPA donor unit to N(Ph-2T-DCV)₃ is effective in improving molecular solubility. Thus, by further introduction m-TPA instead of TPA unit, the one order of magnitude higher hole and electron only mobilities were measured

Table 3
Photovoltaic properties of star-shaped molecules:PC₇₀BM BHJ OSCs, under the illumination of AM 1.5, 100 mW cm⁻².

Donor	D:A [wt%]	V_{oc} [V]	J_{sc} [mA cm ⁻²]	FF [%]	PCE ^a [%]
N(Ph-2T-Rh-Et) ₃	1:3	0.96	9.1	45.6	4.0(3.9)
N(Ph-2T-DCV) ₃ ^b	1:2	0.94	6.6	39.1	2.4(2.3)
N(Ph-OMe-2T-Rh-Et) ₃	1:4	0.92	8.6	50.3	4.0(3.8)
N(Ph-OMe-2T-DCV) ₃ ^c	1:2.5	0.90	8.5	46.6	3.6(3.4)

^a Best values; the average values of PCEs calculated from over six cells are given in brackets.

^b Data from Ref. [9].

^c Data from Ref. [26].

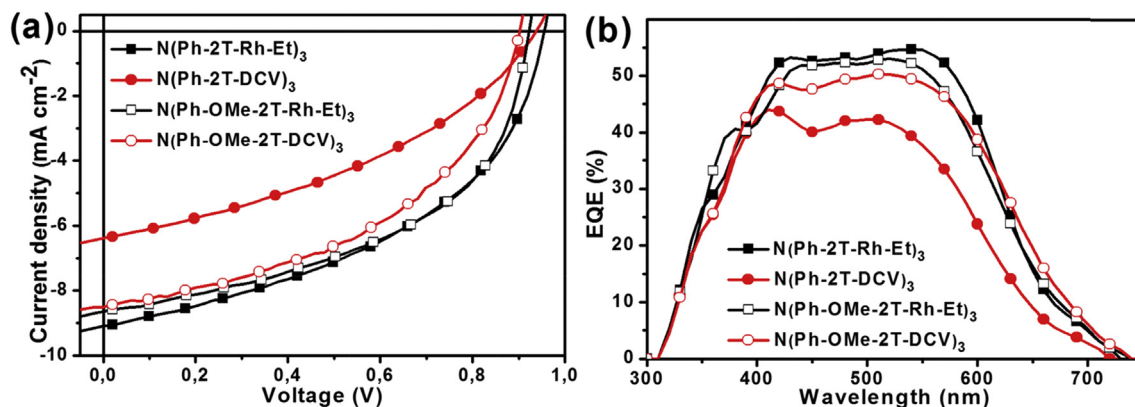


Fig. 5. *J*-*V* curves (a) and EQE spectra (b) of solar cells based on N(Ph-2T-Rh-Et)₃:PC₇₀BM (1:3, wt%), N(Ph-2T-DCV)₃:PC₇₀BM (1:2, wt%), N(Ph-OMe-2T-Rh-Et)₃:PC₇₀BM (1:4, wt%), N(Ph-OMe-2T-DCV)₃:PC₇₀BM (1:2.5, wt%), respectively.

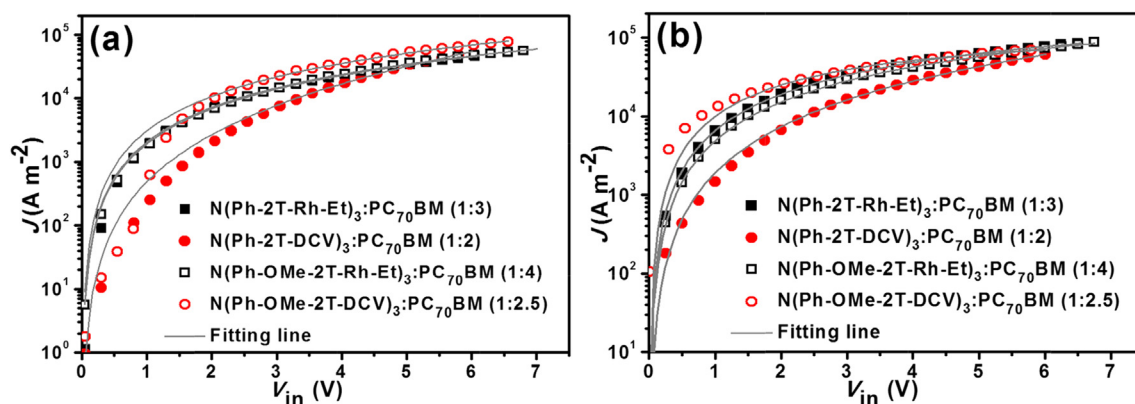


Fig. 6. The dark *J*-*V* characteristics of these star-shaped molecules based diodes including hole (a) and electron (b) only mobilities. The solid lines represent the best fitting using the SCLC modified Mott-Gurney model.

Table 4

Hole and electron only mobilities of blended films with four star-shaped molecules determined from the SCLC measurements.

Blended films	Thickness (nm)	μ_h^a [$\text{cm}^2 \text{V}^{-1} \text{s}^{-1}$]	Thickness (nm)	μ_e^a [$\text{cm}^2 \text{V}^{-1} \text{s}^{-1}$]	μ_e/μ_h
N(Ph-2T-Rh-Et) ₃ :PC ₇₀ BM	75	4.34×10^{-4}	81	1.73×10^{-3}	3.99
N(Ph-2T-DCV) ₃ :PC ₇₀ BM ^b	80	7.98×10^{-5}	70	2.5×10^{-4}	3.13
N(Ph-OMe-2T-Rh-Et) ₃ :PC ₇₀ BM	75	4.09×10^{-4}	80	1.18×10^{-3}	2.89
N(Ph-OMe-2T-DCV) ₃ :PC ₇₀ BM ^c	86	4.58×10^{-4}	75	2.15×10^{-3}	4.69

^a The mobility data reported are average values of the blended films over six diodes.

^b Data from Ref. [9].

^c Data from Ref. [26].

in the N(Ph-OMe-2T-DCV)₃ diodes, as compared to that of N(Ph-2T-DCV)₃. The SCLC data are also in agreement with the photovoltaic parameters of N(Ph-2T-DCV)₃ and N(Ph-OMe-2T-DCV)₃ systems. Besides, the hole and electron mobilities of N(Ph-OMe-2T-Rh-Et)₃ show slightly lower values as compared to the N(Ph-OMe-2T-DCV)₃ system, as seen in Table 4. This correlates well with the difference in their phase behavior, where ordering of N(Ph-OMe-2T-DCV)₃ can be much better as compared to molecules of N(Ph-OMe-2T-Rh-Et)₃ having solubilizing alkyl group at an electron-deficient unit. Nevertheless, N(Ph-OMe-2T-Rh-Et)₃ based device exhibits better FF of 50.3% and thus higher PCE of 4.0% (see Table 3), probably resulting from better balanced charge carrier mobilities (low μ_e/μ_h ratio). Comparison of N(Ph-OMe-2T-Rh-Et)₃ system to that of based on N(Ph-2T-Rh-Et)₃ shows a slightly higher hole and electron mobility of the latter, but the former has more balanced μ_e/μ_h ratio, leading to quite similar photovoltaic performance.

FF of the OSCs depends on a combination of charge extraction and charge recombination rates [37] which relates to the mobility-lifetime product [38]. To take into account the recombination factor, we measured the effective carrier lifetime by transient photovoltage (TPV) technique (Fig. 7). The carrier lifetimes for N(Ph-2T-Rh-Et)₃, N(Ph-OMe-2T-Rh-Et)₃ and N(Ph-OMe-2T-DCV)₃-based blends are similar and demonstrate comparable behavior on the sun intensity to the previously-studied star-shaped molecules [11]. Considering their *J*-*V* characteristics (Fig. 5a), it is not surprising that these systems suffer from non-geminate recombination, even though they show the high charge carrier mobility (Table 4). In addition, the N(Ph-2T-DCV)₃-based system shows higher carrier lifetimes at different light intensities (from 0.1 up to 1 sun), but the carrier mobilities are by more than a factor of 5 lower as compared to the other three systems (Table 4). As a result, N(Ph-2T-Rh-Et)₃, N(Ph-OMe-2T-Rh-Et)₃ and N(Ph-OMe-2T-DCV)₃ systems

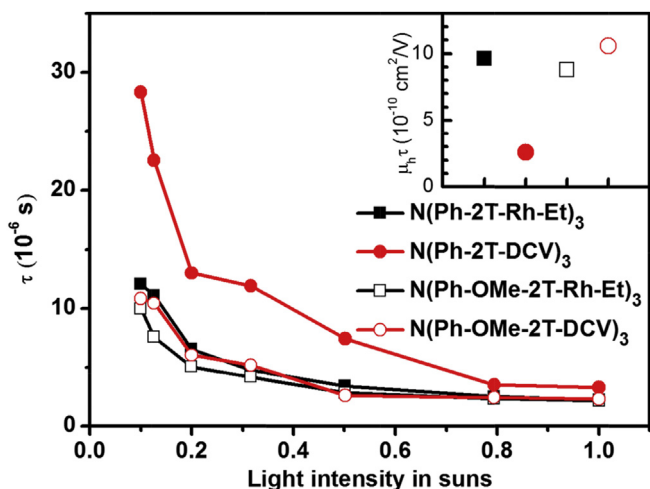


Fig. 7. Charge carrier lifetime as obtained by transient photovoltage technique for the photovoltaic blends based on different molecules (indicated). The inset shows the respective mobility-lifetime products at 1 sun illumination.

demonstrate similar mobility-lifetime products, while for the N(Ph-2T-DCV)₃ system it is considerably lower (Fig. 7, inset). Therefore, the low FF value for the latter system is explained as unbalanced rates of charge extraction and charge recombination, which is most probably rooted in the non-optimal film morphology.

2.6. Ultrafast charge separation

Apart from the charge transport and recombination in BHJ blends, another important factor that impact photovoltaic performance is the efficiency of the initial (i.e. within the first nanosecond) photon-to-charge conversion in the BHJ active layer. To examine the effect of donor and acceptor units of star-shaped molecules on the early-time charge separation dynamics, the photovoltaic blends were interrogated with ultrafast photoinduced absorption (PIA) spectroscopy. The blends were excited with an ultrashort visible pump pulse, which mimics the sun illumination while the concentration of photogenerated charges was monitored by polaron absorption (i.e. charge-induced changes in the molecular IR absorption spectra due to deformation of the molecular backbone) [39] by varying of the delay time between the pump and probe pulses.

Representative PIA transients for the studied blends are shown in Fig. 8. All star-shaped donors in blends with PC₇₀BM demonstrate similar behavior, which is consistent with our previous findings [33]. For all blends, a fast build-up of the signal occurs due to immediate formation of charge-transfer (CT) excitons and/or separated charges. At later times, the PIA signal grows with time-scale of ~2 ps, which is attributed to the hole-transfer process from PC₇₀BM to the star-shaped donor molecule [33]. Finally, the signals decay at ~500 ps timescale due to the intramolecular recombination of the CT excitons and/or geminate recombination of the initially separated charges. Both processes lead to a decrease of the amount of the long-lived separated charges thereby impeding the maximal attaining PCE. Note that at higher excitation densities (>20 $\mu\text{J cm}^{-2}$) substantial non-geminate exciton-exciton annihilation was observed which prompted us to limit excitation intensities as such a way to ensure the exciton density of $\sim 3 \cdot 10^{-3} \text{ nm}^{-3}$.

Maximizing the amount of long-lived separated charges is important for the optimization of a good-working device. Insets in Fig. 8 show the efficiency of charge separation as a function of the PC₇₀BM content. Efficiencies were calculated as a ratio of the

amount of the long-lived charges (i.e. the signal amplitude at 1.5–1.8 ns delays) to a maximal amount of charges which is provided by the given molecule (i.e. the maximal amplitude in the series of blends with different PC₇₀BM content, see Ref. [33] for detailed description). The efficiency of charge separation for all donor molecules depends strongly on both PC₇₀BM content and the particular donor molecule structure. At the optimal PC₇₀BM contents the blends provide up to 60% of long-lived separated charges, which perfectly matches the values of EQE for the OSCs (Fig. 5b). Importantly, for all donor molecules, the optimal PC₇₀BM content for ultrafast charge separation directly correlates with the optimal blend composition for the OSCs (see Table 3). This indicates optimized performance at both the ultrafast sub-ns timescale (i.e. maximized amount of the long-lived charges) and the ultraslow timescale at which the device operates.

At the optimal PC₇₀BM concentration, the blends behave quite similarly at the ultrafast timescales, providing about 50–60% of long-lived charges. However, there are some important differences in the initial growth of the PIA signal. Noticeably, for the N(Ph-2T-Rh-Et)₃ and N(Ph-OMe-2T-Rh-Et)₃ molecules that demonstrate the best performance in devices, there is a prominent delayed build-up of the transients at a ps timescale that is more suppressed at the other two transients. This initial growth is attributed to the diffusion-delayed splitting of PC₇₀BM excitons [33], so that in blends based on N(Ph-2T-DCV)₃ and N(Ph-OMe-2T-DCV)₃ no PC₇₀BM exciton diffusion is observed. The absence of such exciton diffusion may be caused by either of the two scenarios. First, the PC₇₀BM domains in BHJ blends are too large (larger than the exciton diffusion length of ~10 nm) so that the excitons cannot make it to the interface and therefore produce no charges [40]. Second, intermixing of the donor and PC₇₀BM phases is too fine, with the typical scale that is much lower than exciton diffusion length, which leads to almost instantaneous dissociation of the PC₇₀BM excitons. Large PC₇₀BM domains cause decreased contribution of the PC₇₀BM excitons to the overall photocurrent. However, no signs of this are observed in the EQE spectra (Fig. 5b) which shapes look essentially similar for all blends. Therefore, contributions of the donor and PC₇₀BM to the photocurrent are comparable for all molecules.

Fine intermixing, in turn, would not affect the EQE shape, since both donor and PC₇₀BM excitons split with high efficiency. However, very small domain sizes imply extremely large interfacial area in the BHJ films and, most probably, lack of intercalated pathways to the corresponding electrodes. Such nanomorphology leads to the increased non-geminate recombination and decreased charge extraction, which explains low FF and J_{sc} values of the devices based on the N(Ph-2T-DCV)₃ and N(Ph-OMe-2T-DCV)₃ molecules (Fig. 5a, Table 3). In contrast, in the well-performing blends based on N(Ph-2T-Rh-Et)₃ and N(Ph-OMe-2T-Rh-Et)₃ the PC₇₀BM cluster sizes seem to be more optimal, i.e. close to ~10 nm. In this case the clusters are hardly detectable by standard AFM due to its limited spatial resolution and/or poor contrast between the donor and PC₇₀BM domains.

3. Conclusions

In summary, we synthesized the first representatives of D- π -A star-shaped molecules with alkyl-Rh groups as acceptor units. These molecules having either TPA or m-TPA donor core were comprehensively studied and compared to their full analogs with DCV units as the other type of frequently used acceptor units. Usage of 3-ethylrhodanine group having an aliphatic tail leads to a slight decrease of the intermolecular interactions resulting in a more disordered phase state of the star-shaped molecules. However, this does not result in a significant decrease of the hole and electron

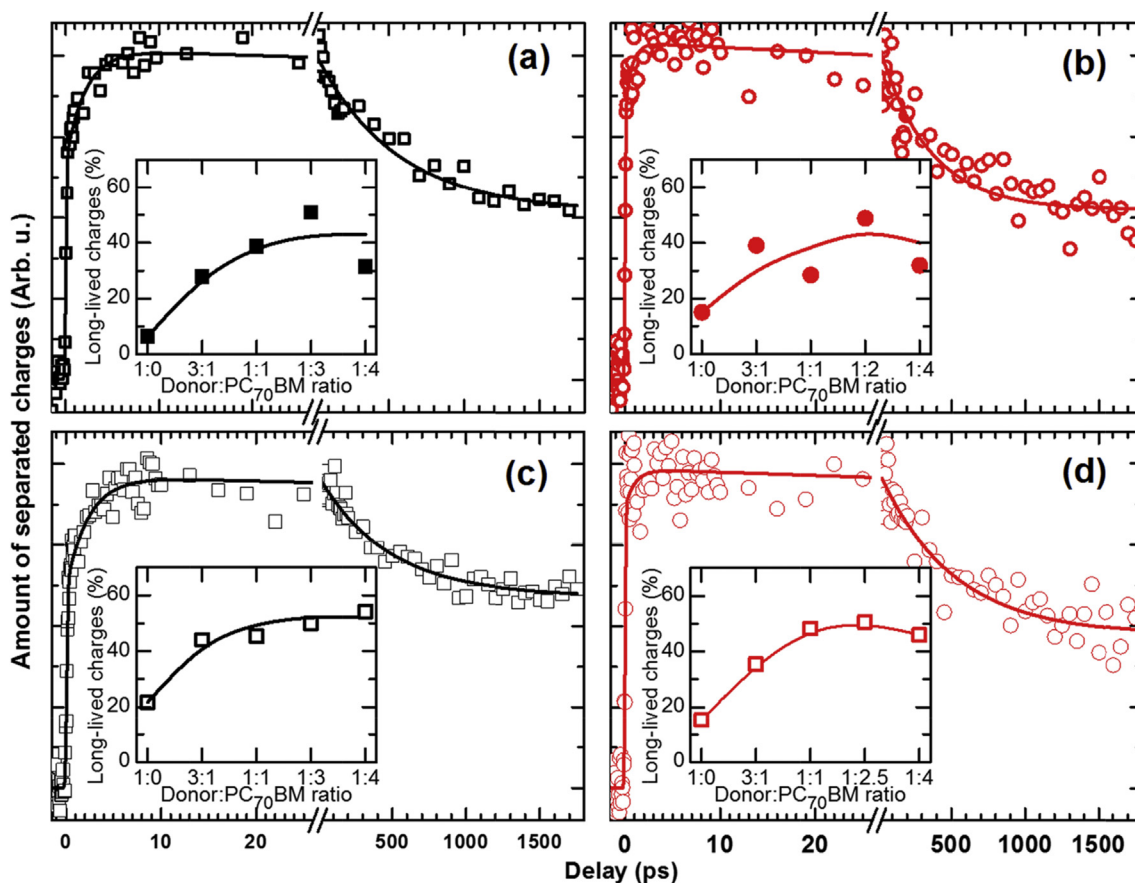


Fig. 8. PIA transients for (a) N(Ph-2T-Rh-Et)₃:PC₇₀BM (1:3, wt%), (b) N(Ph-2T-DCV)₃:PC₇₀BM (1:2, wt%), (c) N(Ph-OME-2T-Rh-Et)₃:PC₇₀BM (1:4, wt%), (d) N(Ph-OME-2T-DCV)₃:PC₇₀BM (1:2.5, wt%), respectively, after excitation at the wavelengths of 550 nm. Symbols represent the experimental data while solid lines show the best multiexponential fits (Eq. S1), with the fit parameters given in Table S2 (see Supporting Information for more details). The insets show the dependence of the efficiency of generation of long-lived charges on PC₇₀BM concentration.

mobilities for their films blended with PC₇₀BM. Meanwhile, the aliphatic tail increases solubility of the molecules with alkyl-Rh groups. Apart from the alkyl-Rh group, usage of m-TPA core instead of common TPA unit can also increase the solubility of the molecules together with their crystallinity. Despite similar morphology of the blended films as observed by AFM, these molecules demonstrate different photovoltaic performance in BHJ OSCs. The star-shaped molecules with 3-ethylrhodanine group show somewhat higher V_{oc} and FF values, and thus higher PCEs in OSCs as compared to their analogs with DCV groups. Among these devices, the N(Ph-2T-DCV)₃ system shows the least optimized device performance resulting from the lowest mobility-lifetime product demonstrated by SCLC and TPV techniques. From the ultrafast charge dynamics, we conclude that this is most likely due to the nonoptimal nanomorphology of the DCV-based blends, which leads to increased bimolecular recombination and less effective carrier extraction. Therefore, alkyl-Rh acceptor group seems to be a favorable choice to design star-shaped molecules for efficient organic photovoltaics.

4. Experimental section

4.1. Materials

Tris(4-bromophenylamine), tetrakis(triphenylphosphine)palladium (0) Pd(PPh₃)₄, malononitrile were obtained from Sigma–Aldrich Co. and used without further purification. THF and toluene were purified according to the known techniques and then

used as solvents. Pyridine was dried and purified according to the known techniques and then used as a solvent. 5,5-dimethyl-2-[5'-(4,4,5,5-tetramethyl-1,3,2-dioxaborolan-2-yl)-2,2'-bithien-5-yl]-1,3-dioxane (**1**), tris{4-[5'-(5,5-dimethyl-1,3-dioxan-2-yl)-2,2'-bithien-5-yl]-2-methoxyphenyl}amine (**3b**), tris[4-(5'-formyl-2,2'-bithiophene-5-yl)-2-methoxyphenyl]amine (**4b**) were obtained as described in Ref. [26]. Tris(4-bromo-2-methoxyphenyl)amine (**2b**) was obtained as described in Ref. [25]. N-ethylrhodanine was prepared as described elsewhere [41]. All reactions, unless stated otherwise, were carried out under an inert atmosphere.

4.2. Synthesis of the star-shaped molecules

Tris{4-[5'-(5,5-dimethyl-1,3-dioxan-2-yl)-2,2'-bithien-5-yl]phenyl}amine (**3a**). In an inert atmosphere, degassed solutions of tris(4-bromophenyl)amine (0.92 g, 1.91 mmol) and **1** (2.79 g, 6.87 mmol) in toluene/ethanol mixture (50/5 mL) and 2 M solution of aq. Na₂CO₃ (10.3 mL) were added to Pd(PPh₃)₄ (238 mg, 0.2 mmol). The reaction mixture was stirred under reflux for 11 h, and then it was cooled to room temperature and poured into 100 mL of water and 100 mL of toluene. The organic phase was separated, washed with water, dried over sodium sulfate and filtered. The solvent was evaporated in vacuum and the residue was dried at 1 Torr. The product was purified by column chromatography on silica gel (eluent toluene: ethyl acetate = 20: 1) to give pure compound **3a** (1.67 g, 81%) as a yellow solid. M.p. = 247–248 °C. ¹H NMR (250 MHz, CDCl₃): δ [ppm] 0.8 (s, 9H), 1.28 (s, 9H), 3.61 (d, 6H, $J = 11$ Hz), 3.74 (d, 6H, $J = 11$ Hz), 5.61 (s,

3H), 7.01–7.06 (overlapping peaks, 6H), 7.09–7.17 (overlapping peaks, 12H), 7.46 (d, 6H, $J = 8.54$ Hz). Calcd (%) for $C_{60}H_{57}NO_6S_6$: C, 66.70; H, 5.32; N, 1.30; S, 17.80. Found: C, 66.57; H, 5.33; N, 1.27; S, 17.81. MALDI-MS: found m/z 1080.63; calculated for $[M]^+$ 1080.51.

Tris[4-(5-formyl-2,2'-bithiophen-5-yl)phenyl]amine (**4a**). 1 M HCl (3 mL) was added to a solution of compound **3a** (0.84 g, 0.8 mmol) in THF (20 mL) and then the reaction mixture was stirred for 4 h at reflux. During the reaction, the product was gradually formed as an orange precipitate. After completion of the reaction the organic phase was separated using diethyl ether, washed with water and filtered off to give pure compound **4a** (0.607 g, 95%) as orange crystals. M.p.: 145–146 °C. 1H NMR (250 MHz, $CDCl_3$): δ [ppm] 7.14 (d, 6H, $J = 8.7$ Hz), 7.21 (d, 3H, $J = 3.7$ Hz), 7.25 (d, 3H, $J = 3.7$ Hz), 7.32 (d, 3H, $J = 4.3$ Hz), 7.51 (d, 6H, $J = 8.7$ Hz), 7.66 (d, 3H, $J = 4.3$ Hz), 9.85 (s, 3H). Calcd (%) for $C_{45}H_{27}NS_6$: C, 65.75; H, 3.31; N, 1.70; S, 23.40. Found: C, 65.88; H, 3.27; N, 1.66; S, 23.30. MALDI-MS: found m/z 820.25; calculated for $[M]^+$ 821.03.

Tris(4-[5'-(3-ethyl-2-thioxothiazolidin-4-one)methyl]-2,2'-bithien-5-yl)phenyl]amine ($N(Ph-2T-Rh-Et)_3$). Compound **4a** (0.480 g, 0.6 mmol), 3-ethylrhodanine (0.56 g, 3.5 mmol) and dry pyridine (15 mL) were placed in a reaction vessel and stirred under argon atmosphere for 14 h at 108 °C using the microwave heating. After completeness of the reaction, pyridine was evaporated under reduced pressure and the residue was dried at 1 Torr. The crude product was purified by column chromatography on silica gel (eluent chloroform). Further purification by precipitation of the product from its THF solution with toluene and hexane led to pure product as a black solid (0.365 g, 50%). 1H NMR (250 MHz, $CDCl_3$): δ [ppm] 1.25 (t, 9H, $J = 7.00$ Hz), 4.10–4.24 (overlapping peaks, 6H), 6.85 (d, 3H, $J = 8.85$ Hz), 7.06–7.15 (overlapping peaks, 6H), 7.19–7.25 (overlapping peaks, 6H), 7.28–7.34 (dd, 6H, $J_1 = 3.7$ Hz, $J_2 = 4.0$ Hz), 7.52 (d, 3H, $J = 8.85$ Hz), 7.82 (s, 3H). ^{13}C NMR (125 MHz, $CDCl_3$): δ [ppm] 12.23, 39.86, 114.71, 118.31, 120.25, 123.52, 124.46, 124.78, 124.89, 126.35, 129.62, 134.44, 135.30, 136.18, 136.83, 145.52, 145.62, 148.19, 167.14, 191.75. Calcd (%) for $C_{60}H_{42}N_4O_3S_{12}$: C, 57.57; H, 3.38; N, 4.48; S, 30.74. Found: C, 57.49; H, 3.29; N, 4.41; S, 30.70. MALDI-MS: found m/z 1251.92; calculated for $[M]^+$ 1251.79.

Tris(4-[5'-(3-ethyl-2-thioxothiazolidin-4-one)methyl]-2,2'-bithien-5-yl)-2-methoxyphenyl]amine ($N(Ph-OMe-2T-Rh-Et)_3$). This compound was prepared according to the procedure described above for $N(Ph-2T-Rh-Et)_3$ using **4b** (0.500 g, 0.5 mmol), 3-ethylrhodanine (0.403 g, 2.7 mmol) and dry pyridine (17 mL) to give pure product as a black solid (0.480 g, 65%). 1H NMR (250 MHz, $CDCl_3$): δ [ppm] 1.28 (t, 9H, $J = 7.00$ Hz), 3.68 (s, 9H), 4.08–4.27 (overlapping peaks, 6H), 6.85 (d, 3H, $J = 8.9$ Hz), 7.05–7.16 (overlapping peaks, 6H), 7.20–7.25 (overlapping peaks, 6H), 7.27–7.35 (dd, 6H, $J_1 = 3.7$ Hz, $J_2 = 4.0$ Hz), 7.82 (s, 3H). ^{13}C NMR (125 MHz, $CDCl_3$): δ [ppm] 12.23, 39.86, 55.90, 109.74, 118.31, 120.25, 123.52, 124.46, 124.78, 124.89, 126.35, 129.62, 134.44, 135.30, 136.18, 136.83, 145.52, 145.62, 153.08, 167.14, 191.75. Calcd (%) for $C_{63}H_{48}N_4O_6S_{12}$: C, 56.39; H, 3.61; N, 4.18; S, 28.67. Found: C, 56.35; H, 3.65; N, 4.19; S, 28.70. MALDI-MS: found m/z 1341.88; calculated for $[M]^+$ 1341.92.

4.3. Characterization

1H NMR spectra were recorded in a “Bruker WP-250 SY” spectrometer, working at a frequency of 250.13 MHz and utilising $CDCl_3$ signal (7.25 ppm) as the internal standard. ^{13}C NMR spectra were recorded using a “Bruker Avance II 300” spectrometer at 75 MHz. In the case of 1H NMR spectroscopy, the compounds to be analysed were taken in the form of 1% solutions in $CDCl_3$. In the case of ^{13}C NMR spectroscopy, the compounds to be analysed were taken in the form of 5% solutions in $CDCl_3$. The spectra were then processed

on the computer using the ACD Labs software. In the case of column chromatography, silica gel 60 (“Merck”) was taken.

Mass-spectra (MALDI) were registered on Autoflex II Bruker (resolution FWHM 18,000), equipped with a nitrogen laser (work wavelength 337 nm) and time-of-flight mass-detector working in reflections mode. The accelerating voltage was 20 kV. Samples were applied to a polished stainless steel substrate. Spectrum was recorded in the positive ion mode. The resulting spectrum was the sum of 300 spectra obtained at different points of sample. 2,5-Dihydroxybenzoic acid (DHB) (Acros, 99%) and α -cyano-4-hydroxycinnamic acid (HCCA) (Acros, 99%) were used as matrices. Elemental analysis of C and H elements was carried out using CHN automatic analyzer CE 1106 (Italy). The settling titration using $BaCl_2$ was applied to analyse sulphur. Experimental error for elemental analysis is 0.30–0.50%. Solubility was measured in ODCB using previously described technique [35]. The Knövenagel condensation was carried out in the microwave synthesizer “Discovery”, (CEM corporation, USA), using a standard method with the open vessel option, 50 W.

Thermogravimetric analysis was carried out in dynamic mode in 30 ÷ 900 °C interval using Mettler Toledo TG50 system equipped with M3 microbalance allowing measuring the weight of samples in 0–150 mg range with 1 μ g precision. Heating/cooling rate was chosen to be 10 °C/min. Every compound was studied twice: in air and in nitrogen flow of 200 mL/min. DSC scans were obtained with Mettler Toledo DSC30 system with 10 °C/min heating/cooling rate in temperature range of +20–290 °C for all compounds. N_2 flow of 50 mL/min was used. Cyclic voltammetry measurements were carried out using solid compact layers of the oligomers, which were prepared by electrostatically rubbing the materials onto a glassy carbon electrode using IPC-Pro M potentiostat. Measurements were made in acetonitrile solution using 0.1 M Bu_4NPF_6 as supporting electrolyte. The scan rate was 200 mV s^{-1} . The glassy carbon electrode was used as a work electrode. Potentials were measured relative to a saturated calomel electrode (SCE). Solution CV measurements were done in 1,2-dichlorobenzene/acetonitrile (4:1) mixture of solvents for 10^{-3} M solutions in a standard three-electrode cell equipped with a glassy carbon working electrode ($s = 2$ mm²), platinum plate as the counter electrode, and SCE (saturated calomel electrode) as the reference electrode. The highest occupied molecular orbital (HOMO) and the lowest unoccupied molecular orbital (LUMO) energy levels were calculated using the first standard formal oxidation and reduction potentials obtained from CV experiments in films according to the following equations: $LUMO = e(\varphi_{red} + 4.40)(eV)$ and $HOMO = -e(\varphi_{ox} + 4.40)(eV)$ [42].

Absorption profiles were recorded with a Perkin Elmer Lambda-35 absorption spectrometer from 350 to 1100 nm. AFM measurements were performed with a Nanosurf Easy Scan 2 in contact mode. Single carrier devices were fabricated and the dark current-voltage characteristics measured and analysed in the space charge limited (SCL) regime. The structures of hole only and electron only devices were Glass/ITO/PEDOT:PSS/semiconductor layer/ MoO_3 (15 nm)/Ag (100 nm) and Glass/ITO/ ZnO /semiconductor layer/ Ca (15 nm)/Ag (100 nm). The detailed procedure for SCLC measurement can be found in Ref. [43].

4.4. Fabrication and characterization of the OSCs

All the devices were fabricated in the normal architecture. Photovoltaic devices were fabricated by doctor-blading on indium tin oxide (ITO)-covered glass substrates (from Osram). These substrates were cleaned in toluene, acetone, and isopropyl alcohol. After drying, the substrates were bladed with 40 nm PEDOT:PSS (Heraeus Deutschland GmbH & Co. KG, PEDOT PH-4083).

Photovoltaic layers, consisting of four different small molecules were dissolved in ODCB with PC₇₀BM as acceptor with various weight ratios, and bladed on top of PEDOT:PSS layer. The thicknesses of these blends are ca. 80–90 nm. After that, a ZnO layer (25 nm) was doctor-bladed on top of the active layer. Finally, an aluminum top electrode of 100 nm thickness was evaporated. The typical active area of the investigated devices was 10.4 mm². The current density voltage characteristics of solar cells were measured under AM1.5G irradiation on an OriSol 1A Solar simulator (100 mW cm⁻²). The EQE was detected with Cary 500 Scan UV-Vis-NIR Spectrophotometer under monochromatic illumination, which was calibrated with a mono-crystalline silicon diode.

4.5. PIA measurements

For the PIA experiments, five blend films of each star-shaped molecules (SSMs) with different SSM:PC₇₀BM weight ratio (from 1:0 to 1:4, see Table S1) were prepared. For films preparation, each star-shaped molecule and PC₇₀BM (obtained from Solenne BV) were dissolved separately in ODCB. Solutions were stirred on a magnetic stirrer for at least 12 h at 50 °C. For blends, each star-shaped molecule solution was mixed with PC₇₀BM solution at the prescribed ratio. Mixed solutions were again stirred for at least 1 h at 50 °C. The films were spin-coated from solutions (700 rpm, 2 min) on microscope cover-glass substrates.

In the PIA measurements, we closely follow the pump-probe arrangement and data processing protocol developed for similar star-shaped materials [33]. In brief, the dynamics of photo-generated charges were tracked using the concept of polaron absorption [44]. The wavelength of the pump pulse was chosen of 550 nm, in accordance with absorption spectra of the studied materials (Fig. 3). The probe wavelengths were chosen near the peak of the respective polaron spectra, i.e. 1.65 μm for N(Ph-2T-DCV)₃ and N(Ph-OMe-2T-DCV)₃, 2.2 μm for N(Ph-2T-Rh-Et)₃ and 1.8 μm for N(Ph-OMe-2T-DCV)₃.

The PIA transients were measured with pump-probe delay from -2 ps to 1.8 ns with time resolution of ~100 fs. For direct comparison of the amount of generated charges in different blends of the given star-shaped molecule, the signals were normalized by the number of absorbed photons. To compare the relative charge generation efficiencies of blends based on different star-shaped molecules, a unity polaronic yield was assigned to the maximal amplitude amongst all blends of the same star-shaped molecule, and the transients within the series were normalized to this value [33].

Acknowledgements

The authors acknowledge P. V. Dmitryakov (National Research Centre “Kurchatov Institute”) for DSC and TGA data obtained for alkyl-Rh molecules. We also thank Jan Anton Koster and Davide Bartesaghi (both at Zernike Institute for Advanced Materials, University of Groningen, the Netherlands) for their advice on the mobility-lifetime analysis. The part of this work including the design, synthesis and characterization of the oligomers was carried out under financial support from the Russian Science Foundation (grant No14-13-01380). The authors gratefully acknowledge the support of the Cluster of Excellence “Engineering of Advanced Materials” at the University of Erlangen-Nuremberg, which is funded by the German Research Foundation (DFG) within the framework of its “Excellence Initiative”. This work has been also partially funded by the Sonderforschungsbereich 953 “Synthetic Carbon Allotropes”, the Solar Factory of the Future on the Energy Campus Nuremberg for financial support (Bavarian State Grant No. 20-3043.5), and the Bavarian initiative “Solar Technologies go Hybrid”

(SolTech). OVK acknowledges support by “Aurora – Towards Modern and Innovative Higher Education” Programme, and by Russian Foundation for Basic Research, research project No14-02-31632.

Appendix A. Supplementary data

Supplementary data related to this article can be found at <http://dx.doi.org/10.1016/j.orgel.2016.02.027>.

References

- [1] P.D. Frischmann, K. Mahata, F. Würthner, *Chem. Soc. Rev.* 42 (2013) 1847.
- [2] B. Kippelen, J.-L. Bredas, *Energy Environ. Sci.* 2 (2009) 251.
- [3] M.C. Scharber, N.S. Sariciftci, *Prog. Polym. Sci.* 38 (45) (2013) 1929.
- [4] A. Mishra, P. Bauerle, *Angew. Chem. Int. Ed.* 51 (2012) 2020.
- [5] J. Roncali, P. Leriche, P. Blanchard, *Adv. Mater.* 26 (2014) 3821.
- [6] B. Kan, M. Li, Q. Zhang, F. Liu, X. Wan, Y. Wang, W. Ni, G. Long, X. Yang, H. Feng, Y. Zuo, M. Zhang, F. Huang, Y. Cao, T.P. Russell, Y. Chen, *J. Am. Chem. Soc.* 137 (2015) 3886.
- [7] H. Meier, *Angew. Chem. Int. Ed.* 44 (2005) 2482.
- [8] W. Ni, X. Wan, M. Li, Y. Wang, Y. Chen, *Chem. Commun.* 51 (2015) 4936.
- [9] S. Ponomarenko, Y.N. Luponosov, J. Min, A.N. Solodukhin, N. Surin, M. Shcherbina, S.N. Chvalun, T. Ameri, C.J. Brabec, *Faraday Discuss.* 174 (2014) 313.
- [10] D. Ye, X. Li, L. Yan, W. Zhang, Z. Hu, Y. Liang, J. Fang, W.-Y. Wong, X. Wang, *J. Mater. Chem. A* 1 (2013) 7622.
- [11] J. Min, Y.N. Luponosov, A. Gerl, M.S. Polinskaya, S.M. Peregudova, P.V. Dmitryakov, A.V. Bakirov, M.A. Shcherbina, S.N. Chvalun, S. Grigorian, N. Kausch-Busies, S.A. Ponomarenko, T. Ameri, C.J. Brabec, *Adv. Energy Mater.* 4 (2014) 1301234.
- [12] V.S. Gevaerts, E.M. Herzig, M. Kirkus, K.H. Hendriks, M.M. Wienk, J. Perlich, P. Müller-Buschbaum, R.A.J. Janssen, *Chem. Mater.* 26 (2014) 916.
- [13] X. Liu, Y. Sun, L.A. Perez, W. Wen, M.F. Toney, A.J. Heeger, G.C. Bazan, *J. Am. Chem. Soc.* 134 (2012) 20609.
- [14] J. Min, Y.N. Luponosov, D. Baran, S.N. Chvalun, M.A. Shcherbina, A.V. Bakirov, P.V. Dmitryakov, S.M. Peregudova, N. Kausch-Busies, S.A. Ponomarenko, T. Ameri, C.J. Brabec, *J. Mater. Chem. A* 2 (2014) 16135.
- [15] N.F. Montcada, L. Cabaua, C.V. Kumar, W. Cambarau, E. Palomares, *Org. Electron* 20 (2015) 15–23.
- [16] (a) C.-Y. Huang, W.-H. Lee, R.-H. Lee, *RSC Adv.* 4 (2014) 48150; (b) S.-Y. Shiau, C.-H. Chang, W.-J. Chen, H.-J. Wang, R.-J. Jeng, R.-H. Lee, *Dyes Pigments* 115 (2015) 35.
- [17] N.D. Eisenmenger, G.M. Su, G.C. Welch, C.J. Takacs, G.C. Bazan, E.J. Kramer, M.L. Chabinyc, *Chem. Mater.* 25 (2013) 1688.
- [18] G.C. Welch, R.C. Bakus, S.J. Teat, G.C. Bazan, *J. Am. Chem. Soc.* 135 (2013) 2298.
- [19] (a) K. Sun, Z. Xiao, S. Lu, W. Zajaczkowski, W. Pisula, E. Hanssen, J.M. White, R.M. Williamson, J. Subbiah, J. Ouyang, A.B. Holmes, W.W.H. Wong, D.J. Jones, *Nat. Commun.* 6 (2015) 6013; (b) C.H. Cui, X. Guo, J. Min, B. Guo, X. Cheng, M.J. Zhang, C.J. Brabec, Y.F. Li, *Adv. Mater.* 27 (2015) 7469, <http://dx.doi.org/10.1002/adma.201503815>; (c) Y. Liu, C.-C. Chen, Z. Hong, J. Gao, Y. Yang, H. Zhou, L. Dou, G. Li, Y. Yang, *Sci. Rep.* 3 (2013) 3356.
- [20] J. Roncali, P. Leriche, A. Cravino, *Adv. Mater.* 19 (2007) 2045.
- [21] E. Ripaud, Y. Olivier, P. Leriche, J. Cornil, J. Roncali, *J. Phys. Chem. B* 115 (2011) 9379.
- [22] P.J. Skabara, J.-B. Arlin, Y.H. Geerts, *Adv. Mater.* 25 (2013) 1948.
- [23] Y. Zhou, W. Chen, Z. Du, D. Ouyang, L. Han, L. Han, R. Yang, *Sci. China Chem.* 58 (2015) 357.
- [24] Y.N. Luponosov, A.N. Solodukhin, S.A. Ponomarenko, *Polym. Sci. Ser. C* 56 (2014) 104.
- [25] J. Min, Y.N. Luponosov, A.N. Solodukhin, N. Kausch-Busies, S.A. Ponomarenko, T. Ameri, C.J. Brabec, *J. Mater. Chem. C* 2 (2014) 7614.
- [26] Y. N. Luponosov, J. Min, A. N. Solodukhin, A. V. Bakirov, P. V. Dmitryakov, M. A. Shcherbina, S. M. Peregudova, G. V. Cherkaev, S. N. Chvalun, C. J. Brabec, S. A. Ponomarenko, 2016, in preparation.
- [27] H. Shang, H. Fan, Y. Liu, W. Hu, Y. Li, X. Zhan, *Adv. Mater.* 23 (2011) 1554.
- [28] P. Zhou, D. Dang, Q. Wang, X. Duan, M. Xiao, Q. Tao, H. Tan, R. Yang, W. Zhu, *J. Mater. Chem. A* 3 (2015) 13568.
- [29] Y. Lin, Z.-G. Zhang, H. Bai, Y. Li, X. Zhan, *Chem. Commun.* 48 (2012) 9655.
- [30] Y.-W. Kao, W.-H. Lee, R.-J. Jeng, C.-F. Huang, J.Y. Wu, R.-H. Lee, *Mater. Chem. Phys.* 163 (2015) 138.
- [31] S. Roquet, A. Cravino, P. Leriche, O. Alevque, P. Frere, J. Roncali, *J. Am. Chem. Soc.* 128 (2006) 3459.
- [32] F. Wu, L. Zhu, S. Zhao, Q. Song, C. Yang, *Dyes Pigments* 124 (2016) 93.
- [33] O.V. Kozlov, Y.N. Luponosov, S.A. Ponomarenko, N. Kausch-Busies, D.Y. Paraschuk, Y. Olivier, D. Beljonne, J. Cornil, M.S. Pshenichnikov, *Adv. Energy Mater* 5 (2015) 1401657.
- [34] Z. Li, G. He, X. Wan, Y. Liu, J. Zhou, G. Long, Y. Zuo, M. Zhang, Y. Chen, *Adv. Energy Mater* 2 (2012) 74.
- [35] J. Min, Y.N. Luponosov, N. Gasparini, L. Xue, F.V. Drodzov, S.M. Peregudova,

- P.V. Dmitryakov, K.L. Gerasimov, D.V. Anokhin, Z.-G. Zhang, T. Ameri, S.N. Chvalun, D.A. Ivanov, Y. Li, S.A. Ponomarenko, C.J. Brabec, *J. Mater. Chem. A* 3 (2015) 22695.
- [36] Y. He, Y. Li, *Phys. Chem. Chem. Phys.* 13 (2011) 1970.
- [37] D. Bartesaghi, I.C. Pérez, J. Kniepert, S. Roland, M. Turbiez, D. Neher, L.J.A. Koster, *Nat. Commun.* 6 (2014) 7083.
- [38] (a) T. Kirchartz, T. Agostinelli, M. Campoy-Quiles, W. Gong, J. Nelson, *J. Phys. Chem. Lett.* 3 (2012) 3470;
(b) A. Baumann, J. Lorrmann, D. Rauh, C. Deibel, V. Dyakonov, *Adv. Mater.* 24 (2012) 4381.
- [39] X. Wei, Z.V. Vardeny, N.S. Sariciftci, *A. J. Phys. Rev. B* 53 (5) (1996) 2187.
- [40] R. Koeppe, N.S. Sariciftci, *Photochem. Photobiol. Sci.* 5 (12) (2006) 1122.
- [41] S. Ravi, K.K. Chiruvella, K. Rajesh, V. Prabhu, S.C. Raghavan, *Eur. J. Med. Chem.* 45 (2010) 2748.
- [42] (a) S.A. Ponomarenko, S. Kirchmeyer, A. Elschner, N.M. Alpatova, M. Halik, H. Klauk, U. Zschieschang, G. Schmid, *Chem. Mater.* 18 (2006) 579;
(b) S.A. Ponomarenko, N.N. Rasulova, Y.N. Luponosov, N.M. Surin, M.I. Buzin, I. Leshchiner, S.M. Peregudova, A.M. Muzafarov, *Macromolecules* 45 (2012) 2014.
- [43] J. Min, Y.N. Luponosov, N. Gasparini, M. Richter, A.V. Bakirov, M.A. Shcherbina, S.N. Chvalun, L. Grodd, S. Grigorian, T. Ameri, S.A. Ponomarenko, C.J. Brabec, *Adv. Energy Mater.* 5 (2015) 1500386.
- [44] X. Wei, Z.V. Vardeny, N.S. Sariciftci, A.J. Heeger, *Phys. Rev. B* 53 (5) (1996) 2187.